In-flight calibration of the XMM-Newton Reflection Grating Spectrometers

C. Erd[a], M. Audard[b], A.J. den Boggende[c], G. Branduardi-Raymont[d], A.C. Brinkman[c], J. Cottam[e], L. Dubbeldam[c], M. Guedel[b], J.W. den Herder[c], J.S. Kaastra[c], S.M. Kahn[e], R. Mewe[c], F.B. Paerels[e], J.R. Peterson[e], A.P. Rasmussen[e], I. Sakelliou[d], J. Spodek[e], K. Thomsen[b], C.P. de Vries[c], A. Zehnder[b]

[a]Astrophysics Division, Space Science Department of ESA, ESTEC, 2200 AG Noordwijk, NL
[b]Paul Scherrer Institute, 5232 Villigen, Switzerland
[c]Space Research Organization of the Netherlands, Sorbonnelaan 2, 3584 CA Utrecht, NL
[d]Mullard Space Science Laboratory, Holmbury St. Mary, Dorking, Surrey, TRH5 6NT, UK
[e]Astrophysics Laboratory, Columbia University, 550 West 120th Street, New York, NY 10027, USA

ABSTRACT

The activities during the instrument calibrations are summarized and first data are presented. The main instrument features, the line-spread function and the effective area, are discussed and the status of the in-flight calibrations is summarized.

Keywords: XMM-Newton, RGS, Spectrometer, X-rays, Calibrations

1. INTRODUCTION

The Reflection Grating Spectrometer (RGS)[1–3] on European Space Agency's (ESA) X-ray observatory XMM-Newton[4] is a dispersive spectrometer which, for the first time in X-ray astronomy, uses reflection gratings as dispersive elements. The main advantage over transmission gratings is their higher dispersion associated with the implementation of grazing incidence to the beam. Grazing incidence reflection gratings offer large dispersion at moderate line spacings, thus delivering high spectral resolving power when coupled with XMM-Newton's moderate angular resolution optics. In addition the gratings can be blazed to produce high reflectivity in a chosen wavelength band. RGS covers the wavelength band from 5 Å (2.5 keV) to 38 Å (330 eV) which encompasses, with the exception of Fe-K, the majority of K and L-shell transitions of elements of astrophysical importance, in particular of the density diagnostics of the helium-like oxygen, neon, magnesium and silicon triplets, and of the Fe-L shells.

RGS comprises two instruments, which are mounted behind two of the three collecting mirrors. Each instrument consists of a reflection grating array that samples about half of the focused light and diffracts it to a secondary focus, the other half being available for two of the three imaging cameras (EPIC[5,6]). Due to the fixed mounting of the grating arrays XMM-Newton provides high resolution dispersive spectroscopy simultaneously with imaging and moderate spectral resolution. The RGS cameras at the secondary foci are equipped with a strip of nine back-illuminated CCD's. These CCD's are elongated and buttable in order to optimize the coverage of the dispersed image. The CCD's are read out in photon counting mode, thus providing each event with the four-fold information of position (X, Y), time and additionally the pulse height. The latter is used to separate the grating diffraction orders and additionally to filter data for background suppression.

The XMM-Newton observatory[4] was successfully launched on December 10, 1999. After an initial out-gasing phase the experiments were switched on during the following month, and the protective covers of the instruments were opened shortly after. For RGS2 and RGS1 this occurred on January 24 and February 6 of this year, respectively. The commissioning of the instruments was followed by a calibration phase, which started on March 10, 2000 and lasted until the end of June.

We summarize the calibration activities and report on first calibration results that have been obtained so far.

2. CALIBRATION MEASUREMENTS

The two results of the calibration efforts are the resolving power, which can be quantified by the Line Spread Function (LSF), and the effective area as a function of wavelength. A set of celestial observations was performed to provide adequate data for the transfer of the ground calibrations to the in-flight conditions (see Table 1). In summary, coronal sources are used for calibrations of dispersion quantities, such as the calibration of the wavelength scale and the LSF, whereas the continuum emission of the remainder of the sources was mainly used for calibrations of the components contributing to the effective area.

Target Name	Observation Type	Purpose
Capella	on-axis	wavelength scale, bore-sight
	in dispersion -10, -5, $+5$, $+10$ arcmin	line-spread function, wavelength scale
	in cross-dispersion -2, $+2$ arcmin	wavelength scale, bore-sight; CTE monitoring
HR1099	on-axis	wavelength scale, bore-sight
	in cross-dispersion $+2$ arcmin	CTE monitoring
Ab Dor	on-axis	wavelength scale, bore-sight confirmation
3C273	on-axis,	effective area; simultaneous with Chandra
	in dispersion -7, $+7$ arcmin	
	in cross-dispersion -1.5, $+1.5$ arcmin	
PKS 2155-304	on-axis	effective area; simultaneous with Chandra
GX13+1	on-axis,	effective area at the short wavelength band
	in dispersion -10, -6, -2, $+2$, $+10$ arcmin	
LMC X-3	on-axis	effective area
Sco X-1	on-axis	CCD gain and CTE; only partly successful

Table 1. Summary of key celestial calibrations.

3. WAVELENGTH SCALE AND BORE-SIGHT

The wavelength scale depends on a number of geometrical properties of the instrument such as

- the angle of the source in the field of view, which determines on the angle of incidence on the gratings
- rotational and translational uncertainties of the Reflection Grating Assembly (RGA), which influences both the angle of incidence and the dispersion angle
- translational uncertainties of the detector along the dispersion direction.

The geometrical dependency of the wavelength scale on these contributions can be obtained from the dispersion equation

$$\frac{m\lambda}{d} = \cos\beta - \cos\alpha \ , \tag{1}$$

with the angle of incidence α and the dispersion angle β, both measured from the surface of the gratings. λ is the incident wavelength which is diffracted into order m, and d is the effective grating line spacing. It follows from differentiation

$$\frac{m\Delta\lambda}{d} = \Delta\alpha\sin\alpha - \Delta\beta\sin\beta \ . \tag{2}$$

The changes $\Delta\alpha$ to the angle of incidence α are a sum of the off-axis angle of the source in dispersion direction, ϕ, and of the (unknown) shifts in the rotation of the RGA around an axis normal to the plane of reflection, χ. Changes of the measured dispersion angle $\Delta\beta$ are a sum of χ plus the angular contribution of shifts (Δz) of the camera in the dispersion direction, which is calculated with the distance between RGA and camera L, as $\Delta z/L$. Therefore

$$\begin{aligned} \Delta\alpha &= \phi + \chi && (3) \\ \Delta\beta &= \chi + \Delta z/L \, . && (4) \end{aligned}$$

After the identification of isolated bright lines in the spectra of the coronal sources (Capella, HR1099, AB Dor) for the first and second orders*, their apparent wavelengths are calculated with starting values of $\Delta\alpha = 0$ and $\Delta\beta = 0$. Under the assumption that these emission lines have the same actual wavelengths as determined by laboratory measurements, the difference is minimized with the free parameters $\Delta\alpha$ and $\Delta\beta$, as for a given wavelength scale ϕ, χ and Δz cannot be uniquely determined.

The goal of the calibrations of the wavelength scale is to calculate $\Delta\alpha$ and $\Delta\beta$ for each calibration observation and to store an appropriate choice of the parameters ϕ, χ and Δz such that the wavelength scale can be predicted for any given combination of source position and satellite attitude on the celestial sphere.

In order to achieve this, a bore-sight axis is defined per instrument relative to the bore-sight axis of the star tracker, which is used for the determination of the satellite's attitude. Three angles are required for a complete definition of the instrument bore-sight axis relative to the star-tracker: an angle along the dispersion direction, one along the cross-dispersion, and the third angle describes rotations around the telescope axis, which is normal to the plane of the field of view. The calculation of the angle along the dispersion is described above and is proportional to ϕ. The angle in the cross-dispersion is straightforwardly obtained from the intensity distribution of the image on the RGS camera. The third angle is determined from shifts of the wavelength scale for observations with a source at large off-axis angles in cross-dispersion direction and from shifts of the image in the cross-dispersion direction for observations with the source at large off-axis angles in dispersion direction.

Details of the internal geometry of the instrument (effecting χ and Δz) are stored in calibration files. The RGS tasks of the XMM-Newton Science Analysis System (SAS)[7] make use of this information and provide the user with a wavelength scale that also is correct for off-axis source positions. Currently the achieved accuracy of the predicted wavelength scale calculated in this way is between 10 mÅ and 20 mÅ. Following further analysis this can probably be reduced to better than 10 mÅ.

4. LINE SPREAD FUNCTION

The line spread function (LSF) of RGS is a convolution of the figure properties of the collecting mirrors (all 58 shells combined) and that of the Reflection Grating Assembly (RGA). The figure property of the RGA depends on the co-alignment and individual distortions of flatness of the 182 grating plates that are integrated per RGA. Apart from these effects there is also a component due to scattering on the surfaces of the mirrors and on the surfaces of the gratings, which is more significant at shorter wavelengths and higher orders of diffraction. Pointing stability of XMM-Newton, which affects the resolving power through variations of the angle of incidence on the gratings has proven to be negligible.

The LSF is sufficiently oversampled by the spatial resolution of the CCD's of the camera. Although the CCD's are buttable, there remain however dead spaces between them of about 0.5 mm (corresponding for first order dispersion to about 85 and 45 mÅ at short and long wavelengths, respectively). Care was taken during the alignment of the instruments to offset the two cameras such that these dead spaces do not coincide in wavelength.

The core of the LSF, which tests the alignment and figure properties of the optical system is best determined from observations of one of the coronal targets, by using an isolated emission line at long wavelength (to avoid distortion of the result due to scattering). The measured data of first order of the O-VIII Lyα emission line are compared with simulations using SciSim[8] and the result is shown in Figure 1. There is good agreement between the measured performance of the LSF and the prediction which is based on pre-flight calibrations. This is summarized in Figure 2 where the measured full widths at half maximum (FWHM) for a set of lines are compared with predictions. This proves that the instrument's resolving power is close to the pre-flight predictions.

*As there is no measurement of the zero order within RGS itself, the wavelength scale has to be derived from the measured positions of known and identified bright lines in first and second orders. The problem is further constrained by using several emission lines at the same time while also requiring consistency between the two main diffraction orders.

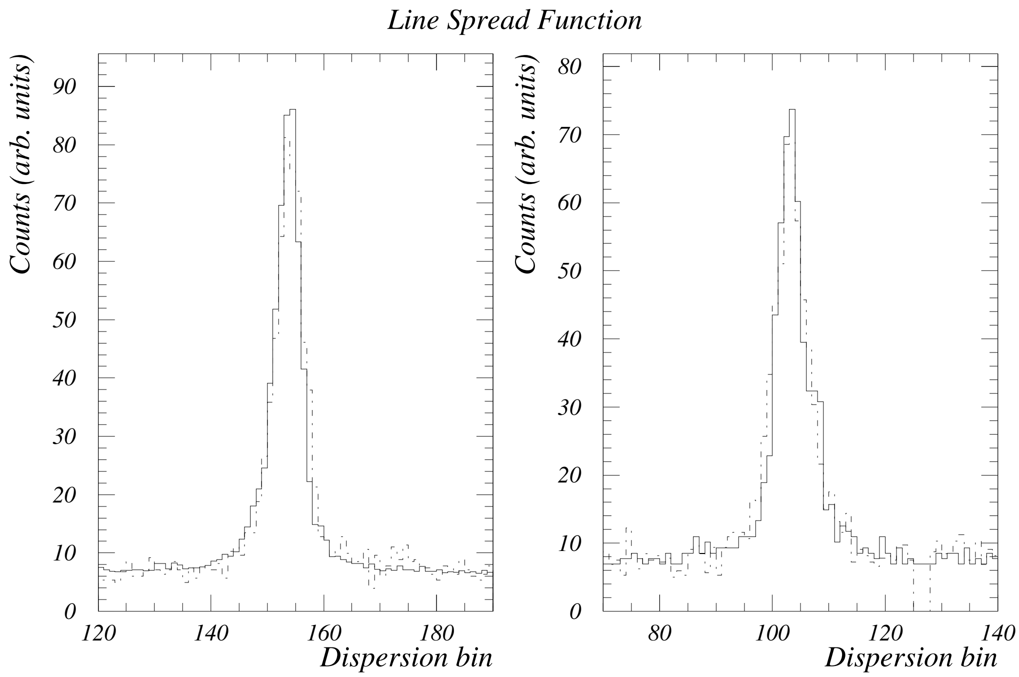

Figure 1. Comparison of Line Spread Functions with pre-flight simulations. The O-VIII Lyα line (18.97 Å) was used to compare data with simulations with SciSim. Data are shown with solid lines, simulations are shown with dash-dotted lines. The LSF for RGS1 is plotted left, that for RGS2 on the right.

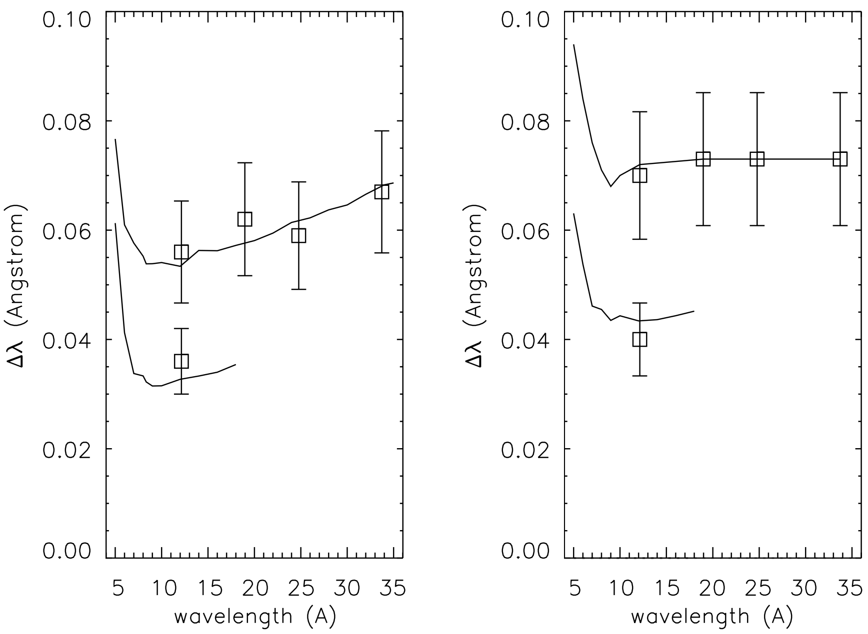

Figure 2. Comparison of measured (squares) and predicted (solid lines) full width at half maximum of the LSF of both RGS instruments for first (larger $\Delta\lambda$) and second orders. Data and predictions for RGS1 are shown left, that for RGS2 on the right.

An example of a dispersed spectrum is shown in Figure 3 of a calibration observation of Capella. A few of the main emission lines are indicated in the plot. A significant fraction of the apparent continuum background measured underneath the Fe-L forest, is due to scattered light.

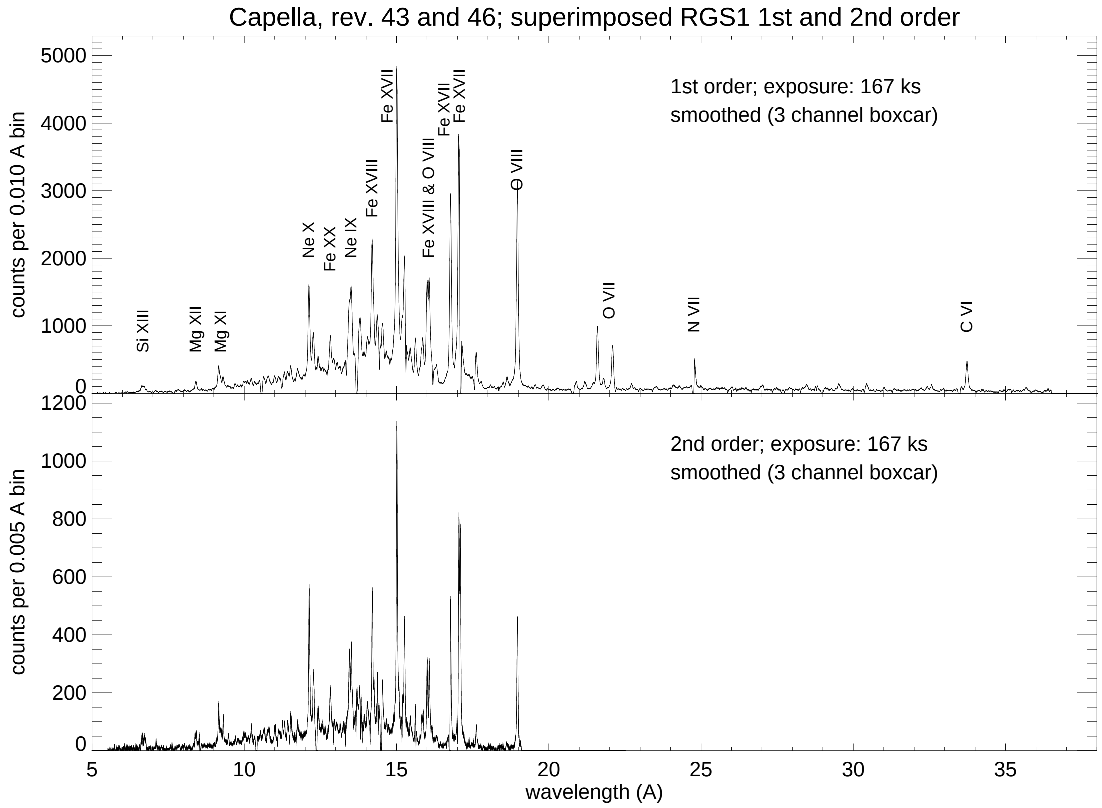

Figure 3. Example of an spectrum of the calibration target Capella measured with RGS1.

5. CCD RESPONSE

The response function of the CCD's is required for order selection and is also used for background rejection. Measurements of the variability of the readout due to thermal noise and potential optical loading have shown good stability with variations of < 1 ADU over time since begin of commissioning.

The gain of the CCD readout nodes was calibrated, starting from pre-flight measured values. Internal calibration sources, which are continuously illuminating the area read out by eight of the total of 18 readout nodes (per camera), were used to calibrate the gains at these nodes. For the remainder of the readout nodes the gains were iteratively improved by using the spectrometer as an energy calibrator where bright known emission lines were used to lock the energy scale and adjusting the gains of the CCD's accordingly. The determined gains were then confirmed with data from the continuum sources GX13+1 and LMC X-3. The final gains, which are slightly different than measured during ground calibrations, were proven to be stable over time to better than 1%.

Monitoring of the charge transfer efficiency (CTE) was performed by observing Capella and HR1099 with off-axis angles in the cross-dispersion direction, close to the edge of the field of view such that the dispersed spectrum falls onto the CCD's at the far side from the readout register. To date no measurable degradation of the CTE is observed. The measured CTE has the same quality as obtained from pre-flight calibration data (1×10^{-5} for parallel transfers, and 4×10^{-5} for the serial register).

The raw measured pulse heights are corrected for losses due to finite CTE, and are converted to gain invariant values (pulse invariant, PI) thus yielding a common pulse height scale as a function of energy for all readout nodes.

PI was used to calibrate a phenomenological model of the redistribution of the response of the CCD's,[1] which includes absorption and charge collection processes in parameterized forms.

The performance of the CCD's impacts on the effective area. For fixed spatial and pulse height filters, uncertainties in the calibration of the CCD response translate into uncertainties in the effective area of RGS associated with those filters. Background rejection and order identification are affected as well.

6. EFFECTIVE AREA

The effective area per diffraction order depends on all optical components that are in the light-path, on the CCD quantum efficiency and on source and order filtering criteria. The following components of the instrument are contributing:

- Mirrors: collecting area and reflectivity (i.e. the effective area of the mirrors)
- RGA:
  - the fraction of collimated light that is intercepted by the RGA
  - the reflectivity of the gratings into the diffraction order
  - the effective surface of the gratings that provides useful diffracted light
    Since the gratings are mounted relatively close together (about 1 cm spacing), light with large dispersion angles is vignetted by the back of the neighboring grating, thus reducing the surface area that provides useful intensity to the camera at these dispersion angles.
- CCD quantum efficiency
  - inactive surface layers (visual light rejection filter Al, and MgF_2 layer)
  - thickness of the active silicon

These components are functions of energy (wavelength) and also source position angle (in the case of mirrors and RGA related components).

In order to reject background, selection of sources is performed by filtering in the imaging domain (cross-dispersion versus dispersion angles). Orders are selected in the CCD pulse height (PI) versus dispersion angle domain. This is shown with an example in Figure 4 with data from a calibration observation of Mkn 421. The upper plot shows the intensity distribution of the image on the camera. Filtering is performed around the strip of the dispersed spectrum, which is indicated by the solid lines in the image. The lower plot shows as a function of dispersion angle the second component of the selection filter together with the various diffraction orders as they are separated by the energy resolution of the CCD's. Low dispersion angle corresponds to shorter wavelengths, higher energies and therefore a higher signal from the CCD's. Several orders (up to four) are easily distinguishable in this plot. The filtering criteria for first and second orders are indicated by solid lines.

With these selections a trade-off has to be made to optimize signal to noise. The user has to be aware of the effects of these selections and should extract spectra with various different widths of these filters to develop an estimate of the amount of background included. Similarly for cases of more than one source in the field of view, selection filters have to be constructed per source. Again by variation of the acceptance of these filters the user can estimate the amount of cross-talk. The width of these selection filters affects the effective area as well.

It is important to note that the same filter that is applied in the image domain, also has to be applied to the exposure map. The exposure map is an image in the time domain, with identical dimensions as the CCD surface elements and holds the active times during which the area of the detectors allows for photon detection. This is then used for construction of the exposure as a function of dispersion bin.

In the order selecting domain, the filter selects a range of allowed CCD pulse heights (PI) as a function of dispersion angle. Since the PI channel number is discrete, the selected PI-range per dispersion bin is a discrete fraction of the total distribution of the CCD response in PI. This effect of discontinuity is included in the response generation by formulation of the CCD response function in PI channels and applying the same filter as for the order selection of data.

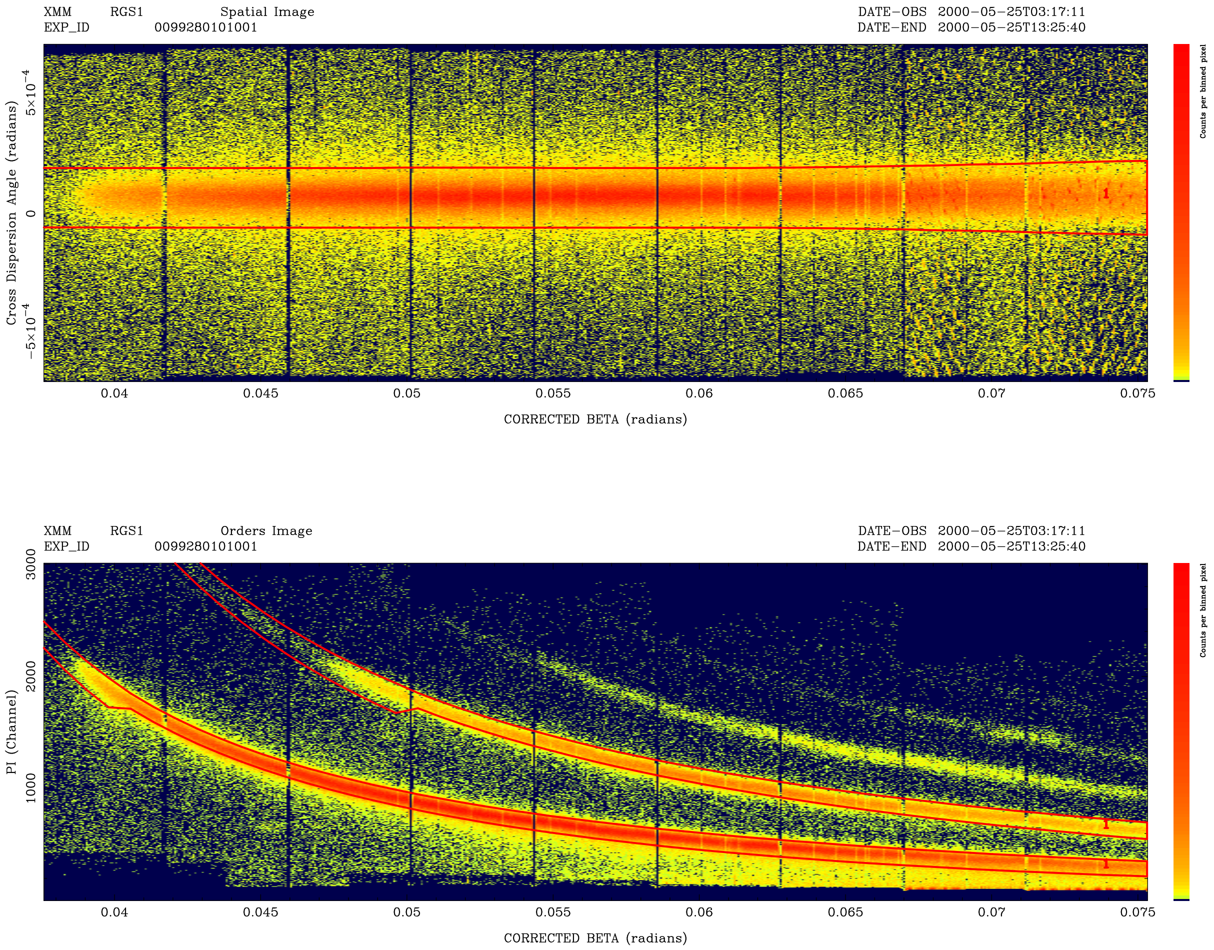

Figure 4. Example of filtering of RGS data. The upper plot shows the image of the dispersed light on the detector (cross-dispersion versus dispersion angles). The lower plot shows the order selection plane, with the CCD's calibrated pulse height (PI) information on the ordinate and the dispersion angle on the abscissa. The solid lines indicate the boundaries of the areas of accepted events chosen by the selection filters. Angular units are radians. Note also that the intensity is scaled logarithmically to also indicate features of low brightness.

As a consequence of the way these filters are applied, the effective area is not a smooth function of wavelength (dispersion angle), but has small scale discontinuities. Due to the consistent application of the filters for data selection and for response generation, these discontinuities are properly included in the modeling of the instrument's response. See[9] for a detailed description of the response generation.

An example of an effective area curve is shown in Figure 5. Sharp features with low efficiency occur at dead spaces of the detector (either due to the gaps between the CCD's, or due to cosmetic blemishes). Due to the large angular extent but low intensity level of the scatter wings of the LSF, the efficiency function around these dead spaces does not completely decrease to zero, and also does not drop sharply. Since the angular size of cosmetic blemishes is smaller than the inter-chip gaps, they cause less loss in effective area.

Additionally there are absorption edges caused by the composition of the inactive surface layers of the CCD's, including silicon (6.74 Å), aluminum (7.95 Å), magnesium (9.52 Å), fluorine (17.80 Å), and oxygen (22.83 Å). Furthermore the small scale discontinuities that were described above can be seen over the entire band pass.

At the time of writing the effective area is still under investigations, but early comparisons with Chandra and EPIC have shown that the effective area is at least to 20% within expectations. However, due to open issues of the precise intensity of the scattered light as a function of wavelength, the uncertainty of the effective area at wavelengths < 7 Å is larger than that.

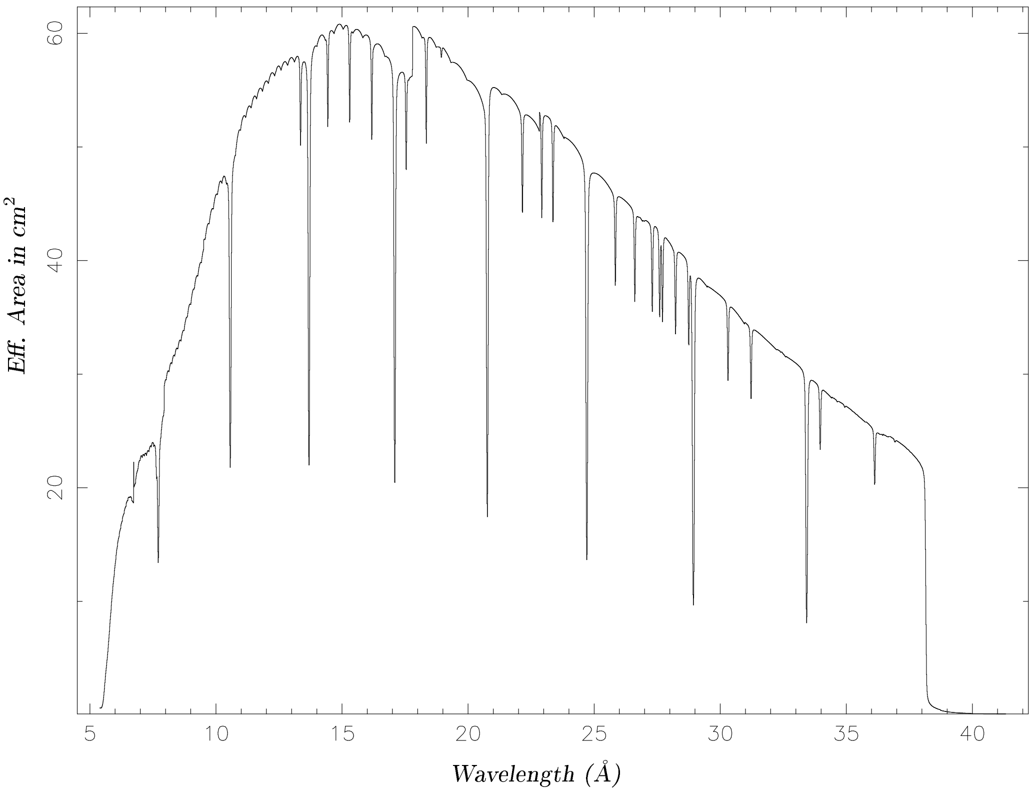

Figure 5. Efficiency function of RGS1 as a function of wavelength. The efficiency is a function of the width of the data selection filters. The chosen width of the selection bands in imaging domain and in the order selecting domain was 90% of the total flux, respectively.

7. CONCLUSIONS

The current calibration provides the wavelength scale with an accuracy of about 10–20 mÅ. A bore-sight transformation is included in the SAS, which calculates the wavelength scale to this accuracy for any source in the RGS field of view. The pre-launch predicted resolving power of the instrument was confirmed.

The gain and CTE of the CCD's are close to pre-launch conditions with good stability and no measurable degradations so far. The measured response function of the CCD's is consistent with data from ground calibrations.

The effective area flight calibration has been limited to checking the relative behavior; the absolute flux calibration remains to be done. However, these preliminary checks on the effective area reveal no inconsistencies with the pre-launch calibration, to the level of about 20%, with indications of a somewhat larger uncertainty at the very shortest wavelengths (< 7 Å).

ACKNOWLEDGMENTS

We greatfully acknowledge the commitment of the operations team which supported the necessary calibration observations. Thanks also go to the members of the SAS development team. XMM-Newton is a mission of the European Space Agency's science program. SRON is financially supported by the Netherlands Organisation for Scientific Research (NWO).

REFERENCES

1. J. W. den Herder, A. J. den Boggende, G. Branduardi-Raymont, A. C. B. J. Cottam, L. Dubbeldam, C. Erd, M. Guedel, J. S. Kaastra, S. M. Kahn, R. Mewe, F. B. Paerels, A. Rasmussen, I. Sakelliou, J. Spodek, K. Thomsen, and C. P. de Vries, "Description and performance of the reflection grating spectrometer on board of XMM-Newton," in *SPIE Proc.*, vol. 4012, 2000.

2. A. C. Brinkman, et al., "The reflection grating spectrometer on board XMM," Proc. of First XMM Workshop, 1998. available at http://xmm.vilspa.esa.es/news/ws1/procs/brinkmanb.pdf.
3. A. C. Brinkman, H. J. Aarts, A. J. den Boggende, T. M. Bootsma, L. Dubbeldam, J. W. den Herder, J. S. Kaastra, P. A. de Korte, B. J. van Leeuwen, R. Mewe, E. J. van Zwet, T. A. Decker, C. J. Hailey, S. M. Kahn, F. B. Paerels, S. M. Pratuch, A. Rasmussen, G. Branduardi-Raymont, P. Guttridge, J. V. Bixler, K. Thomsen, A. Zehnder, and C. Erd, "Reflection grating spectrometer on board XMM," in *SPIE Proc.*, vol. 2808, pp. 463–480, 1996.
4. D. H. Lumb, H. Eggel, R. Laine, and A. J. Peacock, "X-ray multimirror mission: an overview," in *SPIE Proc.*, vol. 2808, pp. 326–337, 1996.
5. A. D. Holland, M. J. L. Turner, A. F. Abbey, and P. J. Pool, "MOS CCDs for the EPIC on XMM," in *SPIE Proc.*, vol. 2808, pp. 414–420, 1996.
6. N. Meidinger, H. W. Brauninger, R. Hartmann, G. Hartner, N. Krause, E. Pferrermann, C. Reppin, G. Schwaab, L. Struder, J. Trumper, P. Holl, J. Kemmer, S. Krisch, H. Soltau, C. van Zanthier, D. Hauf, and R. Richter, "PN-CCD detector for the European Photon Imaging Camera on XMM," in *SPIE Proc.*, vol. 2808, pp. 492–503, 1996.
7. XMM-Newton Science Operations Team, "XMM-Newton science analysis system." to become available at http://xmm.vilspa.esa.es/sas/.
8. XMM-Newton Science Operations Team, "XMM-Newton science simulator SciSim." available at http://xmm.vilspa.esa.es/scisim/scisim.html.
9. A. Rasmussen, et al., "Analysis of real data acquired using the RGS," Proc. of First XMM Workshop, 1998. available at http://xmm.vilspa.esa.es/news/ws1/procs/rasmussena.pdf.